

1 Revision 3

2 Equilibrium Sn isotope fractionation between aqueous Sn and  
3 Sn-bearing minerals: Constrained by first-principles calculations

4 7464

5 Mingguang Sun<sup>1,2</sup>, Ryan Mathur<sup>3</sup>, Caihong Gao<sup>4</sup>, Yanjing Chen<sup>2</sup>, Shunda Yuan<sup>1</sup>, \*

6 <sup>1</sup> China University of Geoscience, Beijing 100083, China

7 <sup>2</sup> MOE Key Laboratory of Orogenic Belts and Crustal Evolution, Peking University,  
8 Beijing 100871, PR China

9 <sup>3</sup> Department of Geology, Juniata College, Huntingdon, PA 16652, USA

10 <sup>4</sup> State Key Laboratory of Ore Deposit Geochemistry, Institute of Geochemistry, Chinese  
11 Academy of Sciences, Guiyang 550081, China

12

13 \*Corresponding author: Shunda Yuan; Email: [shundayuan@cugb.edu.cn](mailto:shundayuan@cugb.edu.cn)

14

15 **Abstract**

16 Equilibrium Sn isotope fractionation properties between aqueous Sn (2+, 4+) species  
17 and Sn-bearing minerals are the key to using tin isotope to trace the transportation,  
18 enrichment and precipitation of tin in various geological processes. However, the  
19 application of Sn isotope geochemistry has been impeded by the absence of equilibrium  
20 Sn isotopic fractionation factors between Sn-bearing minerals and fluid and between  
21 mineral pairs. In this contribution, we conducted first-principles calculations based on the  
22 density functional theory to obtain the equilibrium Sn isotopic fractionation factors

23 between aqueous Sn complexes and minerals. For Sn-bearing complexes in solution, the  
24 reduced partition function ratios ( $\beta$ ) are determined by taking snapshots from the  
25 molecular dynamic trajectories and computing the average  $\beta$  of the snapshots based on  
26 the lowest energy atomic coordinates. For Sn-bearing minerals, the static first-principles  
27 periodic density functional theory methods are performed. The results show that the  $\beta$   
28 factors decrease in the sequence of malayaite<sub>(s)</sub> ( $\text{Sn}^{4+}$ ) > cassiterite<sub>(s)</sub> ( $\text{Sn}^{4+}$ ) >  
29  $\text{Sn}^{4+}\text{Cl}_4(\text{H}_2\text{O})_{2(\text{aq})}$  >  $\text{Sn}^{2+}\text{F}_3^-$  (aq) >  $\text{Sn}^{2+}(\text{OH})_{2(\text{aq})}$  >  $\text{Sn}^{2+}\text{CO}_3(\text{aq})$  > stannite<sub>(s)</sub> ( $\text{Sn}^{4+}$ ) >  
30  $\text{Sn}^{2+}\text{Cl}_3^-$  (aq). The predicted Sn isotope fractionation follows several distinct patterns: (1)  
31 for minerals, the Sn isotope fractionations ( $1000\ln\alpha_{\text{minerals-stannite}}$ ) of cassiterite-stannite  
32 and malayaite-stannite minerals pairs are controlled by the coordination elements of tin,  
33 and equilibrium Sn isotope fractionations factors between mineral pairs are large enough  
34 to make them powerful Sn isotope thermometry; (2) for Sn-bearing aqueous species, the  
35  $\beta$  values of tin (4+) complexes are remarkably larger than those of all aqueous  $\text{Sn}^{2+}$   
36 species, indicating that higher valence tin preferentially enriched heavy tin isotopes. For  
37 aqueous  $\text{Sn}^{2+}$  species, the aqueous species with shorter bonds are enriched in heavy Sn  
38 isotopes than those with longer bonds. When both the valence state and bond length are  
39 different, the valence state is the main factor controlling tin isotope fractionation; (3)  
40 during precipitation of various  $\text{Sn}^{2+}$  aqueous complexes into cassiterite or malayaite,  
41 heavy Sn isotopes tend to be enriched in minerals, while there are two situations for the  
42 precipitation of  $\text{Sn}^{2+}$  complexes into stannite. When Sn is transported in hydrothermal  
43 solution as  $\text{Sn}^{2+}\text{Cl}_3^-$ , stannite precipitation leads to the enrichment of light tin isotopes in  
44 residual solution and late minerals. On the contrary, other  $\text{Sn}^{2+}$  species ( $\text{Sn}^{2+}\text{F}_3^-$ ,  
45  $\text{Sn}^{2+}(\text{OH})_2$  and  $\text{Sn}^{2+}\text{CO}_3$ ) precipitate as stannite will result in the enrichment of heavy tin

46 isotopes in the residual solutions . In addition, the direct precipitation of Sn<sup>4+</sup> complexes  
47 into cassiterite, malayaite, or stannite also produces considerable tin isotope fractionation.  
48 During precipitation, Sn<sup>4+</sup> aqueous complexes form cassiterite or malayaite, and heavy Sn  
49 isotopes tend to be enriched in minerals; while it is precipitated into stannite, heavy Sn  
50 isotopes enrich in residual fluid and late minerals. The calculated results are essential for  
51 further understanding the mechanisms of Sn isotopic fractionation in various Sn-involved  
52 geological processes.

53 Key words: Equilibrium Sn isotope fractionation; First-principles molecular dynamics;  
54 Sn-bearing aqueous species; Sn-bearing minerals

55

56

## 1. INTRODUCTION

57 Tin is an important metal for global high science and the technology industry, and it  
58 has been identified as a critical metal for the development of decarbonization technology  
59 (Moss et al., 2013). Most of the Sn production (99%) throughout the world originates  
60 from hydrothermal tin deposits, and consequently, the ore-forming processes and mineral  
61 exploration of tin have attracted closer attention. (Yuan et al., 2019; Lehmann, 1990, 2021;  
62 Mao et al., 2019, 2021). A great deal of research has shown that Sn (Sn<sup>2+</sup> and Sn<sup>4+</sup>) forms  
63 various complexes with different ligands in different geological fluids (e.g., Tobias, 1958;  
64 Mark, 1977; Pettine et al., 1981; Séby et al., 2001; Müller and Seward, 2001; Uchida et  
65 al., 2002; Duc-Tin et al., 2007; Cigala et al., 2012; Schmidt, 2018; Liu et al, 2020; She et  
66 al., 2020; Wang et al., 2021). According to the limited experimental studies, the Sn  
67 isotope fractionations are obvious among aqueous Sn species and Sn-bearing minerals,  
68 indicating that the Sn isotope geochemistry is a robust tool to trace the Sn-involved

69 geological process (Polyakov et al., 2005; Brugger et al., 2016; Mason et al., 2016;  
70 Badullovich et al., 2017; Creech et al., 2017; Mathur et al., 2017; Yao et al., 2018; Wang  
71 et al., 2019; Liu et al., 2021). The equilibrium Sn isotopic fractionation factors among  
72 Sn-bearing substances are prerequisite to use Sn isotope to trace geological processes.  
73 However, equilibrium Sn isotopic fractionation factors between mineral and fluid and  
74 between mineral pairs are mostly lacking because  $\text{Sn}^{2+}$  is readily oxidized under  
75 environmental conditions (Wang et al., 2019) and dividing  $\text{Sn}^{2+}$  and  $\text{Sn}^{4+}$  complexes in  
76 solutions is tough (Altunay and Gürkan, 2015), which makes it difficult to further decode  
77 the evolution process of Sn in geological systems.

78 Recently, the reduced partition function ratios ( $\beta$  factors) of Sn-Cl species in solution  
79 were preliminary calculated by using the cluster method (one configuration) (She et al.,  
80 2020; Wang et al., 2021; Sun et al., 2022), and the  $\beta$  values of  $\text{Sn}^{2+}$ -Cl species and  
81 tin-bearing minerals (cassiterite, megawite, and romarchite) were calculated by two  
82 different methods: the cluster method and the periodic boundary calculations (Wang et al.,  
83 2021), respectively. However, due to the dynamic property of aqueous solutions, previous  
84 studies have demonstrated that the configuration disorder of the aqueous solutions can  
85 affect the  $\beta$  values (e.g., Li et al., 2009; Li and Liu, 2011; Wang et al., 2019; Gao and Liu,  
86 2021). Therefore, different configurations are required to be sampled when calculating  
87 the  $\beta$  factors for the complexes in solutions. First principles molecular dynamics (FPMD)  
88 simulations based on DFT (Density functional theory) can generate sufficient long and  
89 stable trajectories for solutions at constant volume, temperature and pressure, which can  
90 provide enough configurations to calculate  $\beta$  values of complexes in solutions. This  
91 approach has successfully predicted the equilibrium isotopic fractionation factors among

92 minerals and aqueous species for many isotope systems (e.g., Blanchard et al., 2009,  
93 2017; Kowalski and Jahn, 2011; Dupuis et al., 2015; Qin et al., 2016; Wang et al., 2019;  
94 Gao and Liu, 2021).

95 In the present work, we apply this method to calculate the  $\beta$  values of aqueous Sn  
96 species and tin-bearing minerals. All tin-bearing substances are treated at the same  
97 theoretical level. We focused on  $[\text{Sn}^{2+}(\text{OH})_2]_{(\text{aq})}^0$ ,  $[\text{Sn}^{2+}\text{F}_3]_{(\text{aq})}^-$ ,  $[\text{Sn}^{2+}\text{Cl}_3]_{(\text{aq})}^-$ ,  
98  $[\text{Sn}^{2+}\text{CO}_3]_{(\text{aq})}^0$  and  $[\text{Sn}^{4+}\text{Cl}_4(\text{H}_2\text{O})_2]_{(\text{aq})}$  which have been identified as the predominant  
99 stable Sn-bearing species in various geological fluids (e.g., Mark, 1977; Heinrich, 1990;  
100 Edwards et al, 1996; Sherman et al., 2000; Cigala et al., 2012; Schmidt, 2018; Liu et al,  
101 2020; She et al., 2020; Wang et al., 2021). As for Sn-bearing minerals, we mainly focused  
102 on cassiterite<sub>(s)</sub> ( $\text{Sn}^{4+}\text{O}_2$ ), malayaite<sub>(s)</sub> ( $\text{CaSn}^{4+}\text{SiO}_5$ ) and stannite<sub>(s)</sub> ( $\text{Cu}_2\text{FeSn}^{4+}\text{S}_4$ ) which  
103 are dominant in various types of tin deposits (Hosking, 1988; Eadington, 1983; Eadington  
104 and Kinealy, 1983; Peng and Bromley, 1992; Bortnikov, 2006; Aleksandrov and Troneva,  
105 2007; Yao et al., 2018). The controlling factors of tin isotope fractionation among these  
106 minerals and the aqueous Sn species have been further discussed, and the calculated  
107 equilibrium Sn isotope fractionation between aqueous Sn species and minerals are key to  
108 the utilization of Sn isotopes in geological processes.

109

110

## 2. METHODS

### 111 2.1. Theory

112 Equilibrium Sn isotopic fractionation is determined by the vibrational frequency of  
113 tin atoms in two distinct phases (Bigeleisen and Mayer, 1947; Urey, 1947), and more  
114 details information about the terms and equations of the theory can be found in many

115 reviews (Schauble, 2004; Chacko et al., 2001; Liu et al., 2010; Dauphas and Schauble,  
 116 2016; Blanchard et al., 2017). The isotope exchange reactions of the light tin isotope  
 117 ( $^{116}\text{Sn}$ ) and the heavy tin isotopes ( $^{122}\text{Sn}$  or  $^{124}\text{Sn}$ ) in two tin-bearing substances (SnA and  
 118 SnB):



120 where A and B is a ligand of tin substance. The reduced partition function ratios ( $\beta_{\text{SnA}}$   
 121 or  $\beta_{\text{SnB}}$ ) represent the fractionation factors in two phases (Sn phases of interest and its  
 122 ideal gas atom). The isotope fractionation factor ( $\alpha_{\text{SnA-SnB}}$ ) between the two Sn substances  
 123 (SnA and SnB) can be described by:

$$124 \quad \alpha_{\text{SnA-SnB}} = \beta_{\text{SnA}} / \beta_{\text{SnB}} \quad (2)$$

125 Based on the Bigeleisen-Mayer equation, the  $\beta$  factors is defined as follows  
 126 (Bigeleisen and Mayer, 1947; Urey, 1947):

$$127 \quad \beta = \prod_i^N \frac{u_i^* \exp(-u_i^*/2)[1 - \exp(-u_i)]}{u_i \exp(-u_i/2)[1 - \exp(-u_i^*)]} \quad (3)$$

128 and

$$129 \quad u_i = \frac{h\nu_i}{k_B T} \quad (4)$$

130 Where N depicts the amount of harmonic vibrational modes.  $\nu_i$  depicts the vibrational  
 131 frequency of  $i^{\text{th}}$  mode;  $h$  represents Planck constant;  $k_B$  depicts Boltzmann constant  
 132 and  $T$  depicts the temperature in Kelvin. The above expressions are applicable to the  
 133 calculation of isotope fractionation between molecules.

134 For crystals, the  $\beta$  factor are calculated in a similar way which can be represented  
 135 as following:

$$136 \quad \beta = \left[ \prod_i^N \prod_q \frac{u_{q,i}^* \exp(-u_{q,i}^*/2)[1 - \exp(-u_i)]}{u_{q,i} \exp(-u_i/2)[1 - \exp(-u_i^*)]} \right]^{1/Nq} \quad (5)$$

137

138 where  $N_q$  depicts the amounts of  $q$ -vectors in the Brillouin zone. In this study, the  
139 vibrational frequencies of minerals are achieved by computing supercells. The vibrational  
140 frequencies of  $q = 0$  modes can yield adequately precise  $\beta$  values. Three translational  
141 modes with vibrational frequencies verging on zero are neglected.

142

## 143 **2.2. Computational details**

### 144 **2.2.1. Sn-bearing Minerals**

145 We carried out calculations on cassiterite<sub>(s)</sub> ( $\text{Sn}^{4+}\text{O}_2$ ), malayaite<sub>(s)</sub> ( $\text{CaSn}^{4+}\text{SiO}_5$ ) and  
146 stannite<sub>(s)</sub> ( $\text{Cu}_2\text{FeSn}^{4+}\text{S}_4$ ) (Fig.1). Based on the density functional theory (DFT), the first  
147 principles periodic method is used to calculate the vibrational frequency which is  
148 implemented with Vienna ab initio simulation package (VASP) (Kresse and Furthmüller,  
149 1996). The exchange-correlation functional is defined by the Perdew, Burke and  
150 Ernzerhof (PBE) (Perdew et al., 1996) of generalized gradient approximation (GGA) and  
151 projector augmented wave (PAW) method. The cut-off energy of plane wave is set at 600  
152 eV. On the basis of the Monkhorst-Pack scheme (Monkhorst and Pack, 1976), the k-point  
153 grids in the Brillouin-zone integration are shown in Table 1. Supercells are used for the  
154 structural relaxations (Table 1), and both the cell parameters and atomic positions are  
155 optimized. The force convergence criterion is set as  $10^{-3}$  eV/Å. After relaxations, the  
156 vibration frequencies are computed by applying the density functional perturbation theory  
157 (IBRION=5).

158 In addition, in order to detect the influence of size on Sn isotope fractionation, we  
159 compared the calculated  $\beta$  values with different sizes. For instance, we calculated the  $\beta$   
160 factors of stannite with supercells of  $1 \times 1 \times 1$  and  $2 \times 2 \times 2$ , the calculated  $\beta$  values are

161 1.00323 and 1.00326, respectively. The difference is very small, which indicates that  
162  $2 \times 2 \times 2$  supercells are already large adequately to remove the size effect.

### 163 **2.2.2 Sn-bearing species in aqueous fluids**

164 For aqueous Sn (2+,4+) complexes (Table 1), we carry out the FPMD simulations to  
165 provide configurations for calculating the final  $\beta$  factors. This technique has been used to  
166 predict the Si, Mg, and Br isotope fractionations among various minerals and aqueous  
167 species (Kowalski and Jahn, 2011; Dupuis et al., 2015; Pinilla et al., 2015; Wang et al.,  
168 2019; Gao and Liu, 2021). The simulations of all Sn complexes are carried out in the  
169 NVT (canonical ensemble) thermodynamic ensemble at a fixed temperature of 300K. The  
170 cut-off energy of plane wave is set at 600 eV, and the k-point grids are  $1 \times 1 \times 1$ . For  
171  $[\text{Sn}^{2+}\text{F}_3]^-$  and  $[\text{Sn}^{2+}\text{Cl}_3]^-$  species, the Na atom is added to keep the charge balance. These  
172 cell parameters are selected to guarantee that the statistical pressure is verging on zero  
173 and the densities are nearly  $1 \text{ g/cm}^3$ . The time step for all simulations is set to 1 fs. The  
174 FPMD simulation are totally performed for 50 ps and the energies converge to a constant  
175 value after 30 ps. The Sn-bearing solute molecules and 50 water molecules are embedded  
176 in a cubic box (Table 1). Isotope fractionation has previously been shown to be a  
177 relatively local effect, and fractionations are closely linked to the local structures of the  
178 atoms of interest (e.g., Liu and Tossell, 2005; Li and Liu, 2011; Fujii and Albarede, 2018).  
179 It is sufficient to simulate the local structures of Sn (2+, 4+) ions in solutions using a  
180 solute molecule surrounded by 50 water molecules (e.g., Gao and liu, 2021; Wang et al.,  
181 2019). Because structure after FPMD simulation, with at least 3 layers of water molecules  
182 surrounding the Sn-bearing solute, and each water molecule is in a location that allows  
183 for the formation of two or more hydrogen bonds. They form many four-, five-, and



184 six-member rings (e.g., Xantheas and Dunning, 1993; Estrin et al., 1996; Ludwig and  
185 Weinhold, 1999; Liu and Tossell, 2005).

186 The Sn-bearing species ( $\text{Sn}^{2+}\text{Cl}_3^-(\text{H}_2\text{O})_{50}$ ,  $\text{Sn}^{2+}\text{CO}_3(\text{H}_2\text{O})_{50}$ ,  $\text{Sn}^{2+}(\text{OH})_2(\text{H}_2\text{O})_{50}$ ,  
187  $\text{Sn}^{2+}\text{F}_3^-(\text{H}_2\text{O})_{50}$  and  $\text{Sn}^{4+}\text{Cl}_4(\text{H}_2\text{O})_{50}$ ) solution structures are sustained at 300 K for 50ps  
188 and the energies converge to a constant value between 30ps and 50ps. Because of the  
189 configuration disorder of the aqueous solution, it is necessary to sample enough  
190 configurations to get the converged  $\beta$  value. Here, we take 10 configurations for each  
191 aqueous solution (Fig.2). The configurations are extracted from the equilibrated  
192 trajectories ( $> 30$  ps) with equal intervals (2 ps). Then the atomic positions of the  
193 configurations are optimized with a force convergence criterion of  $1\text{e-}3$  eV/Å. Finally, the  
194 vibration frequencies are calculated to predict the  $\beta$  values for each aqueous species.

195

196

### 3. RESULTS

#### 197 3.1. Structures and $\beta$ factors of minerals

198 The relaxed crystal structures of all calculated minerals are shown in Fig.1. The  
199 calculated lattice parameters of Sn-bearing minerals, bond lengths and frequencies are  
200 listed in Table 1 and Table 2. The  $\beta$  factors of minerals ( $^{124/116}\text{Sn}$  and  $^{122/116}\text{Sn}$ ) are  
201 calculated by equation (5). In Table 3, we present the polynomial fit parameters for the  
202 minerals  $\beta$  factors calculated. The computed  $\beta$  values for cassiterite, malayaite and  
203 stannite are shown in Table S2, and their variation with temperature is shown in Figure 2a.  
204 The  $\beta$  factors of cassiterite and malayaite are much larger than that of stannite. The  
205  $1000\ln(\beta)$  values of cassiterite ( $^{124/116}\text{Sn}$ ) decreased from 11.128 ‰ at 25 °C to 2.666 ‰  
206 at 350 °C, and the  $1000\ln(\beta)$  values of malayaite ( $^{124/116}\text{Sn}$ ) decreased from 11.434 ‰ at

207 25 °C to 2.766 ‰ at 350 °C, and the  $1000\ln\beta$  values of stannite ( $^{124/116}\text{Sn}$ ) decreased from  
208 3.225 ‰ at 25 °C to 0.750 ‰ at 350 °C (Table S2). Malayaite has the shortest Sn-O bond  
209 length and the largest  $1000\ln\beta$  value. Though the tin valence states of the three minerals  
210 are the same (4+), and the coordination number of Sn in stannite (4) is smaller than those  
211 of cassiterite (6) and malayaite (6), the  $1000\ln\beta$  value of stannite is much lower than that  
212 of the other two minerals (Table S2). This is related to the fact that the bonds formed by  
213 Sn and S are much weaker than those formed by Sn and O. Light Sn isotopes are  
214 therefore enriched in Sn-S bonds.

215

### 216 **3.2. Structures and $\beta$ factors of Sn-bearing species in aqueous solutions**

217 In order to evaluate the structural properties of all Sn-bearing aqueous species, we  
218 performed calculations on the partial radial distribution functions (RDFs) of the Sn-O  
219 pair of atoms. The coordination numbers (CNs) for O around Sn and the RDFs of various  
220 Sn aqueous species are shown in Fig.3. Short-range order and long-range disorder are  
221 reflected by the initial peaks and the decrease in magnitude of subsequent fluctuations in  
222 liquids (e.g., Karki, 2010). For  $\text{Sn}^{2+}(\text{OH})_{2(\text{aq})}$ ,  $\text{Sn}^{2+}\text{Cl}_{3^{-}(\text{aq})}$ ,  $\text{Sn}^{2+}\text{CO}_{3(\text{aq})}$  and  $\text{Sn}^{4+}\text{Cl}_{4(\text{aq})}$  at  
223 300 K, the Sn-O RDF peaks occur at  $\sim 2.15$  Å,  $\sim 2.25$  Å,  $\sim 2.15$  Å and  $\sim 1.95$  Å,  
224 respective (Fig. 3). The calculated coordination numbers (CNs) are  $\sim 3.13$ ,  $\sim 1.55$ ,  $\sim 3.89$   
225 and  $\sim 1.07$ , respectively (Fig. 3 inset). For  $\text{SnF}_{3^{-}}$ , at 300 K, there is no sharp peak in the  
226 Sn-O RDF, indicating that  $\text{F}^{-}$  dominates the first shell of  $\text{SnF}_{3^{-}}$ , while water molecules  
227 inhabit the second shell.

228 Ten configurations are extracted from the equilibrated trajectories at equal intervals  
229 of each Sn-bearing species (Fig.2). The  $\beta$  factors are calculated by averaging the  $\beta$  values  
230 of 10 configurations (Table S2; Table S1). The  $\beta$  factors of aqueous Sn species are in

231 order of  $\text{Sn}^{4+}\text{Cl}_4(\text{H}_2\text{O})_2 > \text{Sn}^{2+}\text{F}_3^- > \text{Sn}^{2+}(\text{OH})_2 > \text{Sn}^{2+}\text{CO}_3 > \text{Sn}^{2+}\text{Cl}_3^-$  (Fig. 4b and Table  
232 S2).  $\text{Sn}^{4+}\text{Cl}_4(\text{H}_2\text{O})_2$  has the largest  $\beta$  factors ( $^{124/116}\text{Sn}$ :  $7.627 \pm 0.04$  ‰ at 25 °C), and the  $\beta$   
233 factors of  $\text{Sn}^{2+}\text{Cl}_3^-$  is the smallest ( $^{124/116}\text{Sn}$ :  $2.639 \pm 0.14$  ‰ at 25 °C) (Table S2). In Table  
234 3, we list the polynomial fit parameters for Sn-bearing aqueous species  $\beta$  factors.

235

236

## 4. DISCUSSION

### 237 4.1. Comparison with previous work

238 Previous studies have shown that the nuclear volume effects (NVE), which results  
239 from the isotopic change in the nuclear size and shape, is larger for heavy elements and it  
240 is recognized as the major origin of the mass-independent isotope fractionation  
241 (Bigeleisen, 1996; Schauble, 2007; Abe et al., 2008, 2010; Fujii et al., 2009, 2011, 2013).  
242 For example, the NVE effect is  $\sim 1\%$ /amu (atomic mass unit) for Hg (Schauble, 2007), Pb  
243 (Fujii et al., 2011; Yang and Liu, 2015), TI (Schauble, 2007; Yang and Liu, 2015) and U  
244 (Bigeleisen, 1996; Abe et al., 2008, 2010). Here, the method of applying the  
245 first-principles calculations obtains the mass-dependent fractionation in Sn-bearing  
246 substances resulting from differences in vibrational frequencies, without considering the  
247 effect of NVE on Sn isotope fractionation originating from differences in volume and  
248 shapes of the atomic nuclear. However, according to previous studies, the influence of  
249 NVE on Sn isotope fractionation is usually quite small (0.5‰ in  $^{124/116}\text{Sn}$  for cassiterite  
250 and romarchite at 25°C, 0.14‰ at 727°C) (Schauble, 2013), and therefore the  
251 mass-dependent fractionation at low and moderate temperatures is the main factor leading  
252 to the fractionation of Sn isotopes.

253 Our calculated lattice coefficients of Sn-bearing minerals are well consistent with  
254 the previous experimental values (Table 1) (Brockway, 1934; Takenouchi, 1971; Bolzan et

255 al., 1997). The calculated Sn-O and Sn-S bond length of cassiterite and stannite are 2.059  
256 Å and 2.566 Å, respectively, which are in good agreement with the experimental  
257 measured value, 2.058 Å and 2.539 Å. The calculated of bond length of Si-O, Sn-O and  
258 Ca-O of malayaite (1.647 Å, 2.064 Å and 2.448 Å) are also well consistent with the  
259 experimental measured values (1.641 Å, 2.042 Å and 2.483 Å) (Table 2) (Scott, 1970;  
260 Higgins and Ribbe, 1977; Zhang et al., 1999; Olekseyuk et al., 2002; Fontané et al, 2012;  
261 He et al., 2021). For aqueous Sn species, among different configurations, the variation of  
262  $1000\ln(\beta)$  values are exceeded 0.1 ‰ (Fig.2), indicating that it is essential to sample  
263 different configurations when computing  $\beta$  factors in solution, which is similar to the  
264 previous calculation of Br and Mg species in solution (Wang et al., 2019; Gao and Liu,  
265 2021). In this study, ten configurations are sampled for each aqueous Sn (2+, 4+) species  
266 to calculate the cumulative average values of  $\beta$ , and the values converge to constants  
267 (Fig.2 and Table S2). The  $1000\ln^{122/116}\beta$  values of  $\text{Sn}^{2+}\text{Cl}_3^- \cdot 50\text{H}_2\text{O}$  using the same  
268 theoretical level with the minerals and  $\text{Sn}^{2+}\text{Cl}_3^- \cdot 18\text{H}_2\text{O}$  (one configuration) (Wang et al.,  
269 2021) calculated at B3LYP/def2-TZVP level were 2.07 ‰ and 2.18 ‰, respectively (Fig.  
270 4b and Table S2). For Sn-bearing minerals, the results show that the  $1000\ln^{122/116}\beta$  values  
271 of cassiterite we calculated (PBE) are well consistent with the X-ray scattering (NRIXS)  
272 in synchrotron radiation experiments values (Polyakov et al., 2005) (Fig.4a). The  
273 consistency of these data indicates that our calculation results are accurate and reliable.

274

#### 275 **4.2. Controlling factors on equilibrium Sn isotope fractionation in solution**

276 Based on the calculation, the  $\beta$  values of  $\text{Sn}^{4+}\text{Cl}_4(\text{H}_2\text{O})_2$  are larger than those of  $\text{Sn}^{2+}$   
277 species, indicating that heavy Sn isotopes are preferentially enriched in higher Sn

278 oxidation states, and the enrichment trend is similar to that of Br, Se, and V species in  
279 solution (Li and Liu, 2011; Wu et al., 2015; Gao and Liu, 2021). For the  $\text{Sn}^{2+}$  aqueous  
280 species, the bond lengths of  $\text{Sn}^{2+}\text{-F}_{(\text{aq})}$ ,  $\text{Sn}^{2+}\text{-O}_{(\text{aq})}$  and  $\text{Sn}^{2+}\text{-Cl}_{(\text{aq})}$  are 2.13 Å, 2.14 Å and  
281 2.77 Å, respectively, and the  $\beta$  factors decrease with the increase of bond length (Fig.2b  
282 and Table S2), indicating that bond length is the major controlling factor for the Sn  
283 isotope fractionation of aqueous  $\text{Sn}^{2+}$  species. It conforms to the rule that shorter bonds  
284 have a higher vibrational frequency, which favors enriching heavier isotopes over longer  
285 and weaker bonds (Urey, 1947; Schauble et al., 2004; Young et al., 2009; Huang et al.,  
286 2013, 2014). When the valence states and bond lengths of Sn-bearing species are  
287 different, the valence state has a stronger effect on Sn isotopic fractionation than that of  
288 the bond length among these Sn complexes. For instance, at constant temperature, the  
289 bond length of  $\text{Sn}^{4+}\text{Cl}_4(\text{H}_2\text{O})_2$  (2.44 Å) is longer than those of  $\text{Sn}^{2+}\text{F}_3^-$  (2.13 Å) and  
290  $\text{Sn}^{2+}(\text{OH})_2$  (2.14 Å), but the  $\beta$  factors of  $\text{Sn}^{4+}\text{Cl}_4(\text{H}_2\text{O})_2$  is larger than those of  $\text{Sn}^{2+}\text{F}_3^-$  and  
291  $\text{Sn}^{2+}(\text{OH})_2$  (Fig.2b and Table S2).

292

### 293 **4.3. Sn isotope fractionations among minerals**

294 In previous theoretical studies, a strong correlation has been demonstrated between  $\beta$   
295 values and cell parameters of minerals in equilibrium isotope fractionation of other  
296 elements, such as the valence state of an element (e.g., Schauble et al., 2001), the  
297 coordination number (e.g., Huang et al., 2013; Liu et al., 2018), and the average bond  
298 length (e.g., Huang et al., 2019; Liu et al., 2018; Méheut and Schauble, 2014). For  
299 cassiterite (malayaite) and stannite with different coordination numbers and coordination  
300 elements, heavy tin isotopes are preferentially enriched in cassiterites with high CNs (6),  
301 and light tin isotopes are enriched in stannite with low CNs (4), deviating from the

302 general rule that minerals with low CNs are preferentially enriched in heavy isotopes.  
303 This is because the coordination element of Sn is S in stannite (Sn-S), while the  
304 coordination element of Sn is O in cassiterite and malayaite (Sn-O). The bond strength of  
305 Sn-O is stronger than that of Sn-S, which makes the Sn-O bond length of cassiterite (or  
306 malayaite) shorter than the Sn-S bond length of stannite, suggesting that the properties of  
307 the coordination element have a stronger effect on isotopic fractionation than the  
308 coordination number in these three minerals. The general principle of coordination in  
309 qualitative fractionation factors is also unsuitable for Cu- and Fe-bearing minerals. For  
310 instance, the CNs of Cu in cuprite is two and that of Cu in carbonates and sulfates is four,  
311 but cuprite tends to enrich lighter Cu isotopes than that of carbonates and sulfates (Liu et  
312 al., 2021); the CNs of Fe in chalcopyrite is four, but it is more enriched in lighter Fe  
313 isotope than Fe in hematite and pyrite which CNs is eight (Blanchard et al., 2017).  
314 Although stiff bonds tend to enrich heavy isotopes in various isotopic systems, it is  
315 unclear which of these crystal chemical parameters is the most important factor in  
316 determining the interatomic bonds (Schauble, 2004). This demonstrates the complexity of  
317 factors affecting equilibrium stable isotope fractionation (Liu et al., 2021).

318 In addition, temperature is an important factor influencing the formation of ore  
319 deposits. As a function of temperature, equilibrium stable isotope fractionation among  
320 minerals is a robust tool to reconstruct the thermal evolution process of hydrothermal  
321 deposits. The first-principles calculation provides a reliable method to predict equilibrium  
322 isotope fractionation factors ( $1000\ln\alpha$ ). Recently, a few mineral pairs isotope  
323 geothermometer have been obtained by first-principles calculation, such as Ag  
324 (argentite-stephanite), Mg (garnet-pyroxene, garnet-olive) and Ti (ilmenite-clinopyroxene)

325 (Huang et al., 2013, Wang et al., 2020; Wang et al., 2022). Here, we calculated the  
326 equilibrium Sn isotope fractionation factors among the three minerals (Fig.5) and found  
327 that the Sn isotope fractionation of cassiterite-malayaite varies little ( $1000\ln\alpha_{\text{cassiterite} -}$   
328  $\text{malayaite} \approx 0$ ) with temperature (Fig.5), which indicates that it is not suitable for an isotopic  
329 geothermometer. Cassiterite–stannite and malayaite–stannite, whose  $1000\ln\alpha$  values  
330 show a strong dependence on temperature and vary widely  
331 ( $1000\ln\alpha^{124/116}\text{malayaite-stannite} = 8.209 \text{ ‰}$  and  $1000\ln\alpha^{124/116}\text{cassiterite-stannite} =$   
332  $7.903 \text{ ‰}$  at 25 °C) (Fig. 5). Therefore, cassiterite–stannite and malayaite–stannite have  
333 potential as Sn isotope geothermometers. The tin isotope fractionation of cassiterite–  
334 stannite and malayaite–stannite as functions of temperature is as follows:

335 malayaite-stannite:

$$336 \quad {}^{124/116}\text{Sn} \quad 1000\ln\alpha = (0.57756 \pm 0.00706) \times 10^6/T^2 + (0.67364 \pm 0.03543) \times 10^3/T -$$
$$337 \quad (0.55507 \pm 0.04181)$$

$$338 \quad {}^{122/116}\text{Sn} \quad 1000\ln\alpha = (0.43843 \pm 0.00546) \times 10^6/T^2 + (0.52238 \pm 0.02741) \times 10^3/T -$$
$$339 \quad (0.43413 \pm 0.03234)$$

340 cassiterite-stannite:

$$341 \quad {}^{124/116}\text{Sn} \quad 1000\ln\alpha = (0.58368 \pm 0.00595) \times 10^6/T^2 + (0.52472 \pm 0.02985) \times 10^3/T -$$
$$342 \quad (0.43037 \pm 0.03522)$$

$$343 \quad {}^{122/116}\text{Sn} \quad 1000\ln\alpha = (0.44036 \pm 0.00461) \times 10^6/T^2 + (0.42179 \pm 0.02314) \times 10^3/T - (0.353$$
$$344 \quad \pm 0.0273)$$

345

#### 346 **4.4. Sn isotope fractionation during precipitation processes**

347 The precipitation of various Sn-bearing complexes from hydrothermal solution into  
348 tin-bearing minerals is important for better understanding tin mineralization. According to

349 the calculated results of this study (Fig. 6), the oxidation of  $\text{Sn}^{2+}$  complexes in solution  
350 into  $\text{Sn}^{4+}$ -bearing minerals produces significant tin isotopic fractionation (0 ~ 400 °C)  
351 (Tables 4 and 5), which indicates that the oxidation state of Sn ( $\text{Sn}^{2+}$  aqueous species →  
352  $\text{Sn}^{4+}$  minerals) (except stannite) is the major controlling factor on Sn isotopic  
353 fractionations during precipitation. Therefore, the precipitation of cassiterite or malayaite  
354 from aqueous  $\text{Sn}^{2+}$  complexes (Figs. 6a and 6b) can lead to the enrichment of the lighter  
355 Sn isotope in residual hydrothermal fluid and the later-precipitated Sn-bearing minerals.  
356 This is well consistent with the Sn isotope fractionation in typical tin deposits  
357 investigated by Yao et al. (2018), which show the precipitation of heavy-Sn-enriched  
358 isotope cassiterite results in residual dissolved Sn with lighter isotopic composition in  
359 different types of tin ores.

360 There are two cases of Sn isotope fractionation in the process of precipitation of  
361 these  $\text{Sn}^{2+}$  complexes into stannite (Fig. 6c). When tin transports dominantly as  
362  $[\text{Sn}^{2+}(\text{OH})_2]^0$ ,  $[\text{Sn}^{2+}\text{F}_3]^-$  and  $[\text{Sn}^{2+}\text{CO}_3]^0$ , the precipitation of stannite will lead to the  
363 enrichment of heavy tin isotopes in the residual hydrothermal and later-deposited  
364 minerals. On the contrary, the precipitation of stannite from hydrothermal solution  
365 dominated by  $[\text{Sn}^{2+}\text{Cl}_3]^-$  leads to the enrichment of light tin isotopes in the residual  
366 hydrothermal solution.

367 In addition, recent studies indicate that Sn can also be transported by  $\text{Sn}^{4+}$  aqueous  
368 species (Wang et al., 2021; Schmidt, 2018). For the precipitation process of  $\text{Sn}^{4+}$  species,  
369 our results show that when  $\text{Sn}^{4+}$  precipitates as cassiterite (or malayaite), the values of  
370  $1000\ln(\alpha)[\text{Sn}(\text{IV})\text{Cl}_4(\text{H}_2\text{O})_2]^0\text{-SnO}_2$  ( $^{124/116}\text{Sn}$ ) ranging from -3.479 to -0.834‰ (from 25  
371 to 350 °C) (Tables 4 and 5), which indicate that direct precipitation of  $\text{Sn}^{4+}$  ( $\text{Sn}^{4+}$  aqueous



372 species  $\rightarrow$   $\text{Sn}^{4+}$  mineral) from solution can also cause significant Sn isotope  
373 fractionation. When  $\text{Sn}^{4+}$  precipitates into stannite, it will lead to the enrichment of heavy  
374 tin isotopes in residual hydrothermal and late minerals. The direct precipitation of  $\text{Sn}^{4+}$   
375 species may also be a fractionation mechanism that cannot be ignored in the process of  
376 tin mineralization.  $1000\ln(\alpha)$  values between Sn-bearing aqueous species and minerals at  
377 different temperatures (Fig.5 and Table S3) provide a guideline to understand Sn isotope  
378 fractionations in different geological processes.

379  
380

381

382

## 5. Conclusion and Implication

383 The tin isotope fractionation among Sn aqueous species and minerals are  
384 investigated, and according to the calculated  $\beta$  factors, the enrichment trend of heavy tin  
385 isotopes is malayaite ( $\text{Sn}^{4+}$ ) > cassiterite<sub>(s)</sub> ( $\text{Sn}^{4+}$ ) >  $\text{Sn}^{4+}\text{Cl}_{4(\text{aq})}$  >  $\text{Sn}^{2+}\text{F}_{3^{-}(\text{aq})}$  >  $\text{Sn}^{2+}$   
386  $(\text{OH})_{2(\text{aq})}$  >  $\text{Sn}^{2+}\text{CO}_{3(\text{aq})}$  > stannite<sub>(s)</sub> ( $\text{Sn}^{4+}$ ) >  $\text{Sn}^{2+}\text{Cl}_{3^{-}(\text{aq})}$ . The predominant factors causing  
387 tin isotope fractionation are as follows: (1) for  $\text{Sn}^{2+}$  aqueous species, shorter bonds are  
388 enriched in heavier Sn isotopes relative to longer and weaker bonds, and for Sn(2+, 4+)  
389 aqueous species, the influence of valence state on tin isotope fractionation is stronger  
390 than bond length; (2) for minerals, the properties of coordination elements are the  
391 important factors controlling tin isotope fractionation in the process of tin mineralization,  
392 and malayaite-stannite and cassiterite-stannite, as functions of temperature, have the  
393 potential to be used as geothermometers; (3) and the precipitation of cassiterite or  
394 malayaite leads to the enrichment of light tin isotopes in residual solution and late  
395 minerals, and when stannite precipitates in hydrothermal solution, the fractionation of tin

396 isotopes is controlled by the type of tin complex and valence state, and direct  
397 precipitation of  $\text{Sn}^{4+}$  from hydrothermal solution to  $\text{Sn}^{4+}$  minerals (  $\text{Sn}^{4+}$  species  $\rightarrow$   $\text{Sn}^{4+}$   
398 minerals) also leads to considerable Sn isotope fractionation (0 ~ 400 °C). This study  
399 provides reliable equilibrium Sn isotope fractionation factors among Sn-bearing aqueous  
400 species and minerals, which are key to the potential applications of Sn isotopes in various  
401 geological processes.

## 402 **ACKNOWLEDGEMENTS AND FUNDING**

403 We thank Editor Don Baker and Associate Editor Jianwei Wang for handing the manuscript,  
404 providing insightful comments, and helping to polish the writing. Constructive comments from three  
405 anonymous reviews are appreciated. This study was assisted financially by the National Natural  
406 Science Foundation of China (92062218, 41822304).

407  
408  
409

## 410 **References Cited**

- 411 Abe, M., Suzuki, T., Fujii, Y., and Hada, M. (2008) An ab initio study based on a finite  
412 nucleus model for isotope fractionation in the U (III)–U (IV) exchange reaction  
413 system. *The Journal of chemical physics*, 128(14), 144309.
- 414 Abe, M., Suzuki, T., Fujii, Y., Hada, M., and Hirao, K. (2010) Ligand effect on uranium  
415 isotope fractionations caused by nuclear volume effects: An ab initio relativistic  
416 molecular orbital study. *The Journal of chemical physics*, 133(4), 044309.
- 417 Aleksandrov, S. M., and Troneva, M. A. (2007) Composition, mineral assemblages, and  
418 genesis of titanite and malayaite in skarns. *Geochemistry International*, 45(10):  
419 1012-1024.

- 420 Altunay, N., and Gürkan, R. (2015) An inexpensive and sensitive method for speciative  
421 determination of Sn (IV), Sn (II), and total Sn as Sn (IV) in selected beverages by  
422 micellar improved spectrophotometry. *Food Analytical Methods*, 8(4), 994-1004.
- 423 Badullovich, N., Moynier, F., Creech, J., Teng, F. Z. and Sossi, P. A. (2017) Tin isotopic  
424 fractionation during igneous differentiation and Earth's mantle  
425 composition. *Geochem. Perspect. Lett*, 5, 24-28.
- 426 Bigeleisen, J. (1996) Nuclear size and shape effects in chemical reactions. *Isotope*  
427 *chemistry of the heavy elements*. *Journal of the American Chemical Society*, 118(15),  
428 3676-3680.
- 429 Bigeleisen, J. and Mayer, M. G. (1947) Calculation of equilibrium constants for isotopic  
430 exchange reactions. *The Journal of Chemical Physics*, 15, 261-267.
- 431 Blanchard, M., Balan, E., and Schauble, E. A. (2017) Equilibrium fractionation of  
432 non-traditional isotopes: a molecular modeling perspective. *Reviews in Mineralogy*  
433 *and Geochemistry*, 82, 27-63.
- 434 Blanchard, M., Poitrasson, F., Meheut, M., Lazzeri, M., Mauri, F., and Balan, E. (2009)  
435 Iron isotope fractionation between pyrite (FeS<sub>2</sub>), hematite (Fe<sub>2</sub>O<sub>3</sub>) and siderite  
436 (FeCO<sub>3</sub>): A first-principles density functional theory study. *Geochimica et*  
437 *Cosmochimica Acta*, 73, 6565–6578.
- 438 Bolzan, A. A., Fong, C., Kennedy, B. J., and Howard, C. J. (1997) Structural studies of  
439 rutile-type metal dioxides. *Acta Crystallographica Section B: Structural Science*, 53,  
440 373-380.

- 441 Bortnikov, N. S. (2006) Geochemistry and origin of the ore-forming fluids in  
442 hydrothermal-magmatic systems in tectonically active zones. *Geology of Ore*  
443 *Deposits*, 48, 1-22.
- 444 Brockway, L. O. (1934) The crystal structure of stannite,  $\text{Cu}_2\text{FeSnS}_4$ . *Zeitschrift für*  
445 *Kristallographie-Crystalline Materials*, 89, 434-441.
- 446 Brugger, J., Liu, W., Etschmann, B., Mei, Y., Sherman, D. M. and Testemale, D. (2016) A  
447 review of the coordination chemistry of hydrothermal systems, or do coordination  
448 changes make ore deposits? *Chemical Geology*, 447, 219-253.
- 449 Chacko, T., Cole, D. R., and Horita, J. (2001) Equilibrium oxygen, hydrogen and carbon  
450 isotope fractionation factors applicable to geologic systems. *Reviews in mineralogy*  
451 *and geochemistry*, 43, 1-81.
- 452 Cigala, R. M., Crea, F., De Stefano, C., Lando, G., Milea, D. and Sammartano, S. (2012)  
453 The inorganic speciation of tin (II) in aqueous solution. *Geochimica et*  
454 *Cosmochimica Acta*, 87, 1-20.
- 455 Creech, J. B., Moynier, F., and Badullovich, N. (2017) Tin stable isotope analysis of  
456 geological materials by double-spike MC-ICPMS. *Chemical Geology*, 457, 61-67.
- 457 Dauphas, N., and Schauble, E. A. (2016) Mass fractionation laws, mass-independent  
458 effects, and isotopic anomalies. *Annual Review of Earth and Planetary Sciences*, 44,  
459 709-783.
- 460 Duc-Tin, Q., Audétat, A., and Keppler, H. (2007) Solubility of tin in (Cl, F)-bearing  
461 aqueous fluids at 700 °C, 140 MPa: A LA-ICP-MS study on synthetic fluid  
462 inclusions. *Geochimica et Cosmochimica Acta*, 71, 3323-3335.

- 463 Dupuis, R., Benoit, M., Nardin, E., and Méheut, M. (2015) Fractionation of silicon  
464 isotopes in liquids: The importance of configurational disorder. *Chemical Geology*,  
465 396, 239-254.
- 466 Eadington, P. J. (1983) A fluid inclusion investigation of ore formation in a  
467 tin-mineralized granite, New England, New South Wales. *Economic Geology*, 78,  
468 1204-1221.
- 469 Eadington, P. J., and Kinealy, K. (1983) Some aspects of the hydrothermal reactions of tin  
470 during skarn formation. *Journal of the Geological Society of Australia* 30, 461-471.
- 471 Edwards, R., Gillard, R. D., and Williams, P. A. (1996) The stabilities of secondary tin  
472 minerals. The hydrolysis of tin (II) sulphate and the of  
473  $\text{Sn}_3\text{O}(\text{OH})_2\text{SO}_4$ . *Mineralogical Magazine*, 60, 427-432.
- 474 Estrin, Y. (1996) Dislocation-density-related constitutive modeling. *Unified constitutive*  
475 *laws of plastic deformation*, 1, 69-106.
- 476 Eugster, H. P., and Wilson, G. A. (1985) Transport and deposition of ore-forming  
477 elements in hydrothermal systems associated with granites. In *High heat production*  
478 *(HHP) granites, hydrothermal circulation and ore genesis. Conference* (pp. 87-98).
- 479 Farges, F., Linnen, R. L., and Brown Jr, G. E. (2006) Redox and speciation of tin in  
480 hydrous silicate glasses: a comparison with Nb, Ta, Mo and W. *The Canadian*  
481 *Mineralogist*, 44, 795-810.
- 482 Fontané, X., Izquierdo-Roca, V., Saucedo, E., Schorr, S., Yukhymchuk, V. O., Valakh, M.  
483 Y., and Morante, J. R. (2012) Vibrational properties of stannite and kesterite type  
484 compounds: Raman scattering analysis of  $\text{Cu}_2(\text{Fe}, \text{Zn}) \text{SnS}_4$ . *Journal of Alloys and*  
485 *Compounds*, 539, 190-194.

- 486 Fujii, T., and Albarede, F. (2018)  $^{109}\text{Ag}$ – $^{107}\text{Ag}$  fractionation in fluids with applications to  
487 ore deposits, archeometry, and cosmochemistry. *Geochimica et Cosmochimica Acta*,  
488 234, 37-49.
- 489 Fujii, T., Moynier, F., Agranier, A., Ponzevera, E., Abe, M., Uehara, A., and Yamana, H.  
490 (2013) Nuclear field shift effect in isotope fractionation of thallium. *Journal of*  
491 *Radioanalytical and Nuclear Chemistry*, 296(1), 261-265.
- 492 Fujii, T., Moynier, F., and Albarède, F. (2009) The nuclear field shift effect in chemical  
493 exchange reactions. *Chemical Geology*, 267(3-4), 139-156.
- 494 Fujii, T., Moynier, F., Dauphas, N., and Abe, M. (2011) Theoretical and experimental  
495 investigation of nickel isotopic fractionation in species relevant to modern and  
496 ancient oceans. *Geochimica et Cosmochimica Acta*, 75(2), 469-482.
- 497 Gao, C., and Liu, Y. (2021) First-principles calculations of equilibrium bromine isotope  
498 fractionations. *Geochimica et Cosmochimica Acta*, 297: 65-81.
- 499 He, J., Zhang, H., Yue, T., Sun, W., Hu, Y., and Zhang, C. (2021) Effects of Hydration on  
500 the Adsorption of Benzohydroxamic Acid on the Lead-Ion-Activated Cassiterite  
501 Surface: A DFT Study. *Langmuir*, 37, 2205-2212.
- 502 Heinrich, C. A. (1990) The chemistry of hydrothermal tin (-tungsten) ore  
503 deposition. *Economic Geology*, 85, 457-481.
- 504 Higgins, J. B., and Ribbe, P. H. (1977) The structure of malayaite,  $\text{CaSnOSiO}_4$ , a tin  
505 analog of titanite. *American Mineralogist*, 62, 801-806.
- 506 Hosking, K. F. G. (1988) The world's major types of tin deposit. In *Geology of tin*  
507 *deposits in Asia and the Pacific* (pp. 3-49). Springer, Berlin, Heidelberg.

- 508 Huang, F., Chen, L., Wu, Z., and Wang, W. (2013) First-principles calculations of  
509 equilibrium Mg isotope fractionations between garnet, clinopyroxene,  
510 orthopyroxene, and olivine: implications for Mg isotope thermometry. *Earth and*  
511 *Planetary Science Letters*, 367, 61-70.
- 512 Huang, F., Wu, Z., Huang, S., and Wu, F. (2014) First-principles calculations of  
513 equilibrium silicon isotope fractionation among mantle minerals. *Geochimica et*  
514 *Cosmochimica Acta*, 140, 509-520.
- 515 Huang, F., Zhou, C., Wang, W., Kang, J., and Wu, Z. (2019) First-principles calculations  
516 of equilibrium Ca isotope fractionation: Implications for oldhamite formation and  
517 evolution of lunar magma ocean. *Earth and Planetary Science Letters*, 510, 153-160.
- 518 Karki, B. B. (2010). First-principles molecular dynamics simulations of silicate melts:  
519 structural and dynamical properties. *Reviews in Mineralogy and Geochemistry*, 71,  
520 355-389.
- 521 Kowalski, P. M., and Jahn S. (2011) Prediction of equilibrium Li isotope equilibrium  
522 fractionation between minerals and aqueous solutions at high P and T: an efficient ab  
523 initio approach. *Geochimica et Cosmochimica Acta*, 75, 6112–6123.
- 524 Kresse, G., and Furthmüller J. (1996) Efficiency of ab-initio total energy calculations for  
525 metals and semiconductors using a plane-wave basis set. *Computational materials*  
526 *science*, 6, 15-50.
- 527 Lehmann, B. (1987) Tin granites, geochemical heritage, magmatic differentiation.  
528 *Geologische Rundschau*, 76, 177-185.
- 529 Lehmann, B. (1990) Large-scale tin depletion in the Tanjungpandan tin granite, Belitung  
530 Island, Indonesia. *Economic Geology*, 85, 99-111.

- 531 Lehmann, B. (2006). Metallogeny of tin (Vol. 32). Springer.
- 532 Lehmann, B. (2021) Formation of tin ore deposits: A reassessment. *Lithos*, 402, 105756.
- 533 Li, X., and Liu, Y. (2011). Equilibrium Se isotope fractionation parameters: a  
534 first-principles study. *Earth and Planetary Science Letters*, 304, 113-120.
- 535 Li, X., Zhao, H., Tang, M., and Liu, Y. (2009) Theoretical prediction for several important  
536 equilibrium Ge isotope fractionation factors and geological implications. *Earth and  
537 Planetary Science Letters*, 287, 1-11.
- 538 Liu, P., Mao, J., Lehmann, B., Weyer, S., Horn, I., Mathur, R., and Zhou, Z. (2021) Tin  
539 isotopes via fs-LA-MC-ICP-MS analysis record complex fluid evolution in single  
540 cassiterite crystals. *American Mineralogist*, 106, 1980-1986.
- 541 Liu, Q., Tossell, J. A., and Liu, Y. (2010) On the proper use of the Bigeleisen–Mayer  
542 equation and corrections to it in the calculation of isotopic fractionation equilibrium  
543 constants. *Geochimica et Cosmochimica Acta*, 74, 6965-6983.
- 544 Liu, S., Li, Y., Ju, Y., Liu, J., Liu, J., and Shi, Y. (2018) Equilibrium nickel isotope  
545 fractionation in nickel sulfide minerals. *Geochimica et Cosmochimica Acta*, 222,  
546 1-16.
- 547 Liu, S., Li, Y., Liu, J., Yang, Z., Liu, J., and Shi, Y. (2021) Equilibrium Cu isotope  
548 fractionation in copper minerals: a first-principles study. *Chemical Geology*, 564,  
549 120060.
- 550 Liu, Y., and Tossell, J. A. (2005) Ab initio molecular orbital calculations for boron isotope  
551 fractionations on boric acids and borates. *Geochimica et Cosmochimica Acta*, 69,  
552 3995-4006.



- 553 Liu, Y., Li, J., and Chou, I. M. (2020) Cassiterite crystallization experiments in alkali  
554 carbonate aqueous solutions using a hydrothermal diamond-anvil cell. American  
555 Mineralogist: Journal of Earth and Planetary Materials, 105, 664-673.
- 556 Ludwig, R., Weinhold, F., and Farrar, T. C. (1999) Quantum cluster equilibrium theory of  
557 liquids: molecular clusters and thermodynamics of liquid ethanol. Molecular Physics,  
558 97(4), 465-477.
- 559 Mao, J. W., Yuan, S. D., Xie, G. Q., Song, S. W., Zhou, Q., Gao, Y. B., Liu, X., Fu X. F.,  
560 Cao, J., Zeng Z. L., Li T. G. and Fan, X. Y. (2019) New advances on metallogenic  
561 studies and exploration on critical minerals of China in 21st century. Mineral  
562 Deposits, 38, 935-969.
- 563 Mao, J., Zheng, W., Xie, G., Lehmann, B., and Goldfarb, R. (2021) Recognition of a  
564 Middle–Late Jurassic arc-related porphyry copper belt along the southeast China  
565 coast: Geological characteristics and metallogenic implications. Geology, 49,  
566 592-596.
- 567 Mark, W. (1977) Hydrolysis of the Tin (II) ion,  $\text{Sn}^{2+}$ , in alkaline solution. Acta Chemica  
568 Scandmavica A, 31, 157-162.
- 569 Mason, A. H., Powell, W. G., Bankoff, H. A., Mathur, R., Bulatović, A., Filipović, V. and  
570 Ruiz, J. (2016) Tin isotope characterization of bronze artifacts of the central  
571 Balkans. Journal of Archaeological Science, 69, 110-117.
- 572 Mathur, R., Powell, W., Mason, A., Godfrey, L., Yao, J., and Baker, M. E. (2017)  
573 Preparation and measurement of cassiterite for Sn isotope analysis. Geostandards  
574 and Geoanalytical Research, 41, 701-707.

- 575 Monkhorst, H. J. and Pack, J. D. (1976) Special points for Brillouin-zone  
576 integrations. *Physical review B*, 13, 5188.
- 577 Moss, R. L., Tzimas, E., Willis, P., Arendorf, J., Thompson, P., Chapman, A. and Ostertag,  
578 K. (2013) Critical Metals in the Path towards the Decarbonisation of the EU Energy  
579 Sector. Assessing rare metals as supply-chain bottlenecks in low-carbon energy  
580 technologies. JRC Report EUR, 25994.
- 581 Méheut, M. and Schauble, E. A. (2014) Silicon isotope fractionation in silicate minerals:  
582 insights from first-principles models of phyllosilicates, albite and pyrope.  
583 *Geochimica et Cosmochimica Acta*, 134, 137-154.
- 584 Müller, B., and Seward, T. M. (2001) Spectrophotometric determination of the stability of  
585 tin (II) chloride complexes in aqueous solution up to 300°C. *Geochimica et*  
586 *Cosmochimica Acta*, 65, 4187-4199.
- 587 Olekseyuk, I. D., Gulay, L. D., Dydchak, I. V., Piskach, L. V., Parasyuk, O. V. and  
588 Marchuk, O. V. (2002) Single crystal preparation and crystal structure of the  
589  $\text{Cu}_2\text{Zn}/\text{Cd}$ ,  $\text{Hg}/\text{SnSe}_4$  compounds. *Journal of Alloys and Compounds*, 340, 141-145.
- 590 Peng, Q., and Bromley, A. V. (1992) Fluid inclusion studies of the skarn-type tin  
591 mineralization at Red-A-ven, Northwest Dartmoor, England. *Chinese journal of*  
592 *geochemistry*, 11, 362-369.
- 593 Perdew, J. P., Burke, K., and Ernzerhof, M. (1996) Generalized gradient approximation  
594 made simple. *Physical review letters*, 77, 3865.
- 595 Pettine, M., Millero, F. J., and Macchi, G. (1981) Hydrolysis of tin (II) in aqueous  
596 solutions. *Analytical Chemistry*, 53, 1039-1043.

- 597 Pinilla, C., Blanchard, M., Balan, E., Natarajan, S. K., Vuilleumier, R., and Mauri, F.  
598 (2015) Equilibrium magnesium isotope fractionation between aqueous  $Mg^{2+}$  and  
599 carbonate minerals: Insights from path integral molecular dynamics. *Geochimica et*  
600 *Cosmochimica Acta*, 163, 126-139.
- 601 Polyakov, V. B., Mineev, S. D., Clayton, R. N., Hu, G., and Mineev, K. S. (2005)  
602 Determination of tin equilibrium isotope fractionation factors from synchrotron  
603 radiation experiments. *Geochimica et Cosmochimica Acta*, 69, 5531-5536.
- 604 Qin, T., Wu, F., Wu, Z., and Huang, F. (2016) First-principles calculations of equilibrium  
605 fractionation of O and Si isotopes in quartz, albite, anorthite, and zircon.  
606 *Contributions to Mineralogy and Petrology*, 171, 1-14.
- 607 Roskosz, M., Amet, Q., Fitoussi, C., Dauphas, N., Bourdon, B., Tissandier, L. and Alp, E.  
608 E. (2020) Redox and structural controls on tin isotopic fractionations among  
609 magmas. *Geochimica et Cosmochimica Acta*, 268, 42-55.
- 610 Schauble, E. A. (2004) Applying stable isotope fractionation theory to new  
611 systems. *Reviews in mineralogy and geochemistry*, 55, 65-111.
- 612 Schauble, E. A. (2007) Role of nuclear volume in driving equilibrium stable isotope  
613 fractionation of mercury, thallium, and other very heavy elements. *Geochimica et*  
614 *Cosmochimica Acta*, 71(9), 2170-2189.
- 615 Schauble, E. A. (2013) Modeling nuclear volume isotope effects in crystals. *Proceedings*  
616 *of the National Academy of Sciences*, 110(44), 17714-17719.
- 617 Schauble, E. A., Rossman, G. R., and Taylor Jr, H. P. (2001) Theoretical estimates of  
618 equilibrium Fe-isotope fractionations from vibrational spectroscopy. *Geochimica et*  
619 *Cosmochimica Acta*, 65, 2487-2497.

- 620 Schmidt, C. (2018) Formation of hydrothermal tin deposits: Raman spectroscopic  
621 evidence for an important role of aqueous Sn (IV) species. *Geochimica et*  
622 *Cosmochimica Acta*, 220, 499-511.
- 623 Scott J. F. (1970) Raman spectrum of SnO<sub>2</sub>. *The Journal of Chemical Physics*, 53,  
624 852-853.
- 625 She, J. X., Wang, T., Liang, H., Muhtar, M. N., Li, W., and Liu, X. (2020) Sn isotope  
626 fractionation during volatilization of Sn (IV) chloride: Laboratory experiments and  
627 quantum mechanical calculations. *Geochimica et Cosmochimica Acta*, 269,  
628 184-202.
- 629 Sherman, D. M., Ragnarsdottir, K. V., Oelkers, E. H. and Collins, C. R. (2000) Speciation  
630 of tin (Sn<sup>2+</sup> and Sn<sup>4+</sup>) in aqueous Cl solutions from 25 °C to 350°C: an in-situ  
631 EXAFS study. *Chemical Geology*, 167, 169-176.
- 632 Sun, M., Mathur, R., Chen, Y., Yuan, S. and Wang, J. First-principles Study on  
633 Equilibrium Sn Isotope Fractionations in Hydrothermal Fluids. *Acta Geologica*  
634 *Sinica-English Edition*.
- 635 Séby, F., Potin-Gautier, M., Giffaut, E. and Donard, O. F. X. (2001) A critical review of  
636 thermodynamic data for inorganic tin species. *Geochimica et Cosmochimica*  
637 *Acta*, 65, 3041-3053.
- 638 Takenouchi, S. (1971) Hydrothermal synthesis and consideration of the genesis of  
639 malayaite. *Mineralium Deposita*, 6, 335-347.
- 640 Tobias, R. S. (1958) Studies on the hydrolysis of metal ions. *Acta Chem Scand*, 12,  
641 198-223.

- 642 Uchida, E., Sakamori, T., and Matsunaga, J. (2002) Aqueous speciation of lead and tin  
643 chlorides in supercritical hydrothermal solutions. *Geochemical journal*, 36, 61-72.
- 644 Urey, H. C. (1947) The thermodynamic properties of isotopic substances. *Journal of the*  
645 *Chemical Society (Resumed)*, 562-581.
- 646 Wang, D., Mathur, R., Powell, W., Godfrey, L., and Zheng, Y. (2019) Experimental  
647 evidence for fractionation of tin chlorides by redox and vapor  
648 mechanisms. *Geochimica et Cosmochimica Acta*, 250, 209-218.
- 649 Wang, J. L., Wei, H. Z., Williams-Jones, A. E., Dong, G., Zhu, Y. F., Jiang, S. Y., and Lu,  
650 J. J. (2022) Silver isotope fractionation in ore-forming hydrothermal systems.  
651 *Geochimica et Cosmochimica Acta*, 322, 24-42.
- 652 Wang, T., She, J. X., Yin, K., Wang, K., Zhang, Y., Lu, X. and Li, W. (2021) Sn (II)  
653 chloride speciation and equilibrium Sn isotope fractionation under hydrothermal  
654 conditions: A first principles study. *Geochimica et Cosmochimica Acta*, 300, 25-43.
- 655 Wang, W., Huang, S., Huang, F., Zhao, X. and Wu, Z. (2020) Equilibrium inter-mineral  
656 titanium isotope fractionation: Implication for high-temperature titanium isotope  
657 geochemistry. *Geochimica et Cosmochimica Acta*, 269, 540-553.
- 658 Wang, W., Zhou, C., Liu, Y., Wu, Z. and Huang, F. (2019) Equilibrium Mg isotope  
659 fractionation among aqueous  $Mg^{2+}$ , carbonates, brucite and lizardite: Insights from  
660 first-principles molecular dynamics simulations. *Geochimica et Cosmochimica Acta*,  
661 250, 117-129.
- 662 Wu, F., Qin, T., Li, X., Liu, Y., Huang, J. H., Wu, Z., and Huang, F. (2015)  
663 First-principles investigation of vanadium isotope fractionation in solution and  
664 during adsorption. *Earth and Planetary Science Letters*, 426, 216-224.

- 665 Xantheas, S. S., and Dunning Jr, T. H. (1993) Ab initio studies of cyclic water clusters  
666  $(\text{H}_2\text{O})_n$ ,  $n=1-6$ . I. Optimal structures and vibrational spectra. The Journal of  
667 chemical physics, 99(11), 8774-8792.
- 668 Yang, S., and Liu, Y. (2015) Nuclear volume effects in equilibrium stable isotope  
669 fractionations of mercury, thallium and lead. Scientific reports, 5(1), 1-12.
- 670 Yao, J., Mathur, R., Powell, W., Lehmann, B., Tornos, F., Wilson, M. and Ruiz, J. (2018)  
671 Sn-isotope fractionation as a record of hydrothermal redox reactions. American  
672 Mineralogist, 103, 1591-1598.
- 673 Young, E. D., Manning, C. E., Schauble, E. A., Shahar, A., Macris, C. A., Lazar, C., and  
674 Jordan, M. (2015) High-temperature equilibrium isotope fractionation of  
675 non-traditional stable isotopes: Experiments, theory, and applications. Chemical  
676 Geology, 395, 176-195.
- 677 Young, E. D., Tonui, E., Manning, C. E., Schauble, E., and Macris, C. A. (2009) Spinel-  
678 olivine magnesium isotope thermometry in the mantle and implications for the Mg  
679 isotopic composition of Earth. Earth and Planetary Science Letters, 288, 524-533.
- 680 Yuan, S., Williams-Jones, A. E., Romer, R. L., Zhao, P. and Mao, J. (2019)  
681 Protolith-related thermal controls on the decoupling of Sn and W in Sn-W  
682 metallogenic provinces: Insights from the Nanling region, China. Economic  
683 Geology, 114, 1005-1012.
- 684 Zhang, M., Meyer, H. W., Groat, L. A., Bismayer, U., Salje, E. K. H., and Adiwidjaja, G.  
685 (1999) An infrared spectroscopic and single-crystal X-ray study of malayaite,  
686  $\text{CaSnSiO}_5$ . Physics and Chemistry of Minerals, 26, 546-553.
- 687

688 **Figure and table captions**

689

690 **Figure 1.** Mineral crystal structure calculated in this study: (A) malayaite (supercell

691  $2 \times 1 \times 1$ ), (B) cassiterite (supercell  $2 \times 2 \times 3$ ), and (C) stannite (supercell  $2 \times 2 \times 2$ ).

692

693 **Figure 2.** The calculated  $1000\ln(\beta)$  ( $^{124/116}\text{Sn}$ ) values of 10 configurations (Grey points)

694 and their cumulative average values (Colored points) at 25 °C.

695

696 **Figure 3.** Radial distribution functions (RDFs) for Sn-O pairs of  $\text{Sn}^{2+}(\text{OH})_{2(\text{aq})}$ ,  $\text{Sn}^{2+}\text{Cl}_3^-$

697  $_{(\text{aq})}$ ,  $\text{Sn}^{2+}\text{CO}_3_{(\text{aq})}$ ,  $\text{Sn}^{2+}\text{F}_3^-_{(\text{aq})}$  and  $\text{Sn}^{4+}\text{Cl}_{4(\text{aq})}$ . The insets represent the coordination

698 numbers (CNs) varied with the distance.

699 **Figure 4.** The calculated  $1000\ln(\beta)$  (‰) for (a) minerals and (b) Sn-bearing species in

700 solutions (0 – 400 °C). The  $^{122/116}\text{Sn}$  (cassiterite) and  $^{122/116}\text{SnCl}_3^-$  from Polyakov et al.

701 (2005) and Wang et al. (2021) are also shown for comparison.

702 **Figure 5.** Calculated  $1000\ln\alpha$  values of malayaite-stannite, cassiterite-stannite and

703 malayaite-cassiterite as a function of temperature.

704

705 **Figure 6.**  $1000\ln(\alpha)$  minerals – aqueous species ( $^{124/116}\text{Sn}$  and  $^{122/116}\text{Sn}$ ) (‰). (a)  $1000\ln(\alpha)$

706 aqueous species – cassiterite ( $^{124/116}\text{Sn}$  and  $^{122/116}\text{Sn}$ ); (b)  $1000\ln(\alpha)$  aqueous species –

707 malayaite ( $^{124/116}\text{Sn}$  and  $^{122/116}\text{Sn}$ );  $1000\ln(\alpha)$  aqueous species – stannite ( $^{124/116}\text{Sn}$  and

708  $^{122/116}\text{Sn}$ ).

709

710

711 **Table 1.** Calculation parameters of minerals and aqueous complexes

712

713 **Table 2.** Coordination number and calculated bond length of minerals

714

715 **Table 3.** Polynomial fit parameters for the calculation of tin isotope fractionation factors

716 as  $1000\ln(\beta) = ax + bx^2 + cx^3$ , where  $x = 10^6/T^2$  and T is the temperature in Kelvin

717 (273.15 K to 673.15 K)

718

719

720

721

722

723

724



**Table 1.** Calculation parameters of minerals and aqueous complexes

Model		Lattice parameters						
Minerals	Supercell	k-point grid	a(Å)	b(Å)	c(Å)	$\alpha(^{\circ})$	$\beta(^{\circ})$	$\gamma(^{\circ})$
cassiterite	2×2×3	3×3×3	4.736 (4.737) <sup>a</sup>	4.736 (4.737) <sup>a</sup>	3.187 (3.186) <sup>a</sup>	90	90	90
	2×2×2	3×3×4	4.737	4.737	3.186	90	90	90
malayaite	1×1×1	1×1×1	7.152 (7.150) <sup>b</sup>	8.888(8.890) <sup>b</sup>	6.667 (6.660) <sup>b</sup>	90	113.37	90
	2×1×1	1×1×1	7.152	8.888	6.667			
stannite	1×1×1	3×3×3	5.14 (5.46) <sup>c</sup>	5.414 (5.46) <sup>c</sup>	5.414(5.46) <sup>c</sup>	90	90	90
	2×2×2	1×1×1	5.14	5.414	5.414	90	90	90
Complexes in aqueous solution								
		1×1×1	12.3188	12.3188	12.3188	90	90	90
		1×1×1	12.1474	12.1474	12.1474	90	90	90
		1×1×1	12.0491	12.0491	12.0491	90	90	90
		1×1×1	12.1361	12.1361	12.1361	90	90	90
		1×1×1	12.0491	12.0491	12.0491	90	90	90

Notes: The experimental values which are listed in brackets are compare with the optimized cell parameters.

<sup>a</sup> Bolzan et al.(1997).

<sup>b</sup> Takenouchi, (1971).

<sup>c</sup> Brockway. (1934).

**Table 2.** Coordination number and calculated bond length of minerals

Model		Bond length(Å)	Coordination number	Frequencies(cm-1)
Cassiterite (Sn <sup>4+</sup> O <sub>2</sub> )	Sn-O	2.059(2.058) <sup>a</sup>	6	776(773) <sup>d</sup>
Malayaite (CaSn <sup>4+</sup> SiO <sub>5</sub> )	Si-O	1.647(1.641) <sup>b</sup>	6	951(941) <sup>e</sup>
	Sn-O	2.064(2.042) <sup>b</sup>		
	Ca-O	2.448(2.483) <sup>b</sup>		
Stannite (Cu <sub>2</sub> FeSn <sup>4+</sup> S <sub>4</sub> )	Sn-S	2.566(2.539) <sup>c</sup>	4	346(350) <sup>f</sup>

Notes: Comparison between calculated value and the experimental value which show in brackets.

<sup>a</sup> Bolzan et al.(1997)

<sup>b</sup> Higgins and Ribbe,(1977)

<sup>c</sup> Olekseyuk et al (2002)

<sup>d</sup> Scott (1970)

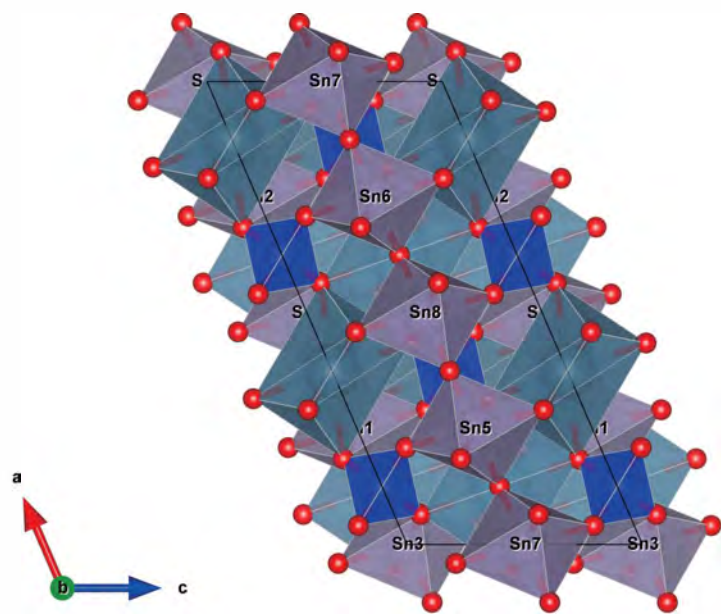
<sup>e</sup> Zhang et al (1999)

<sup>f</sup> Fontané et al (2012)

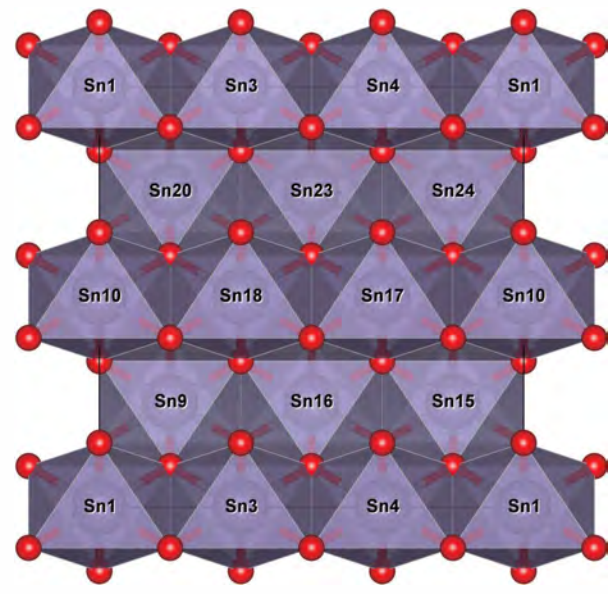
**Table 3.** Polynomial fit parameters for the calculation of tin isotope fractionation factors as  $1000\ln(\beta) = ax + bx^2 + cx^3$ , where  $x = 10^6/T^2$  and T is the temperature in Kelvin (273.15 K to 673.15 K).

Model		a	b	c
Cassiterite	<sup>124/116</sup> Sn	1.0506	-0.00634	7.59E-05
	<sup>122/116</sup> Sn	0.80108	-0.00487	5.68E-06
Malayaite	<sup>124/116</sup> Sn	1.09313	-0.00789	9.40E-05
	<sup>122/116</sup> Sn	0.83357	-0.00614	7.84E-05
Stannite	<sup>124/116</sup> Sn	0.29093	-2.10E-04	-1.58E-05
	<sup>122/116</sup> Sn	0.22286	-4.52E-04	4.40E-06
Sn <sup>2+</sup> Cl <sub>3</sub> <sup>-</sup> ·50H <sub>2</sub> O	<sup>124/116</sup> Sn	0.25039	-9.80E-04	1.43E-05
	<sup>122/116</sup> Sn	0.19085	-7.48E-04	1.10E-05
Sn <sup>2+</sup> CO <sub>3</sub> ·50H <sub>2</sub> O	<sup>124/116</sup> Sn	0.34162	-0.00219	2.78E-05
	<sup>122/116</sup> Sn	0.2607	-0.00182	3.30E-05
Sn <sup>2+</sup> (OH) <sub>2</sub> ·50H <sub>2</sub> O	<sup>124/116</sup> Sn	0.40894	-0.00281	4.06E-05
	<sup>122/116</sup> Sn	0.31107	-0.00195	1.91E-05
Sn <sup>2+</sup> F <sub>3</sub> <sup>-</sup> ·50H <sub>2</sub> O	<sup>124/116</sup> Sn	0.42503	-0.00217	2.25E-05
	<sup>122/116</sup> Sn	0.32389	-0.00166	1.79E-05
Sn <sup>4+</sup> Cl <sub>4</sub> ·50H <sub>2</sub> O	<sup>124/116</sup> Sn	0.72425	-0.00458	5.59E-05
	<sup>122/116</sup> Sn	0.5518	-0.00346	4.15E-05

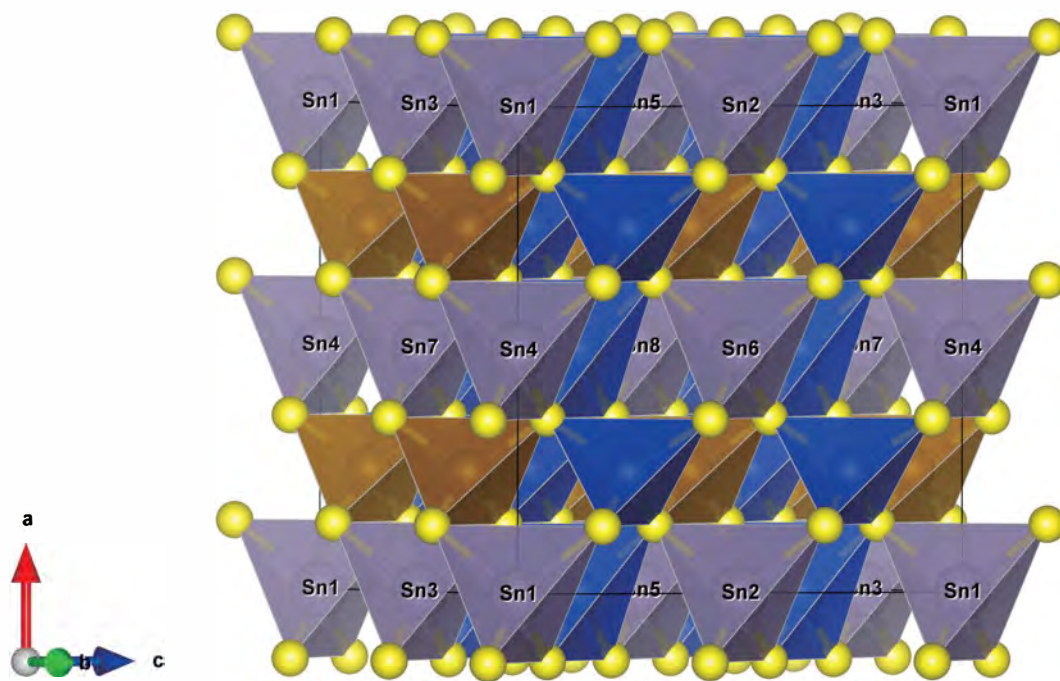
Fig.1



(A) malayaite



(B) cassiterite



(C) stannite

Fig.2

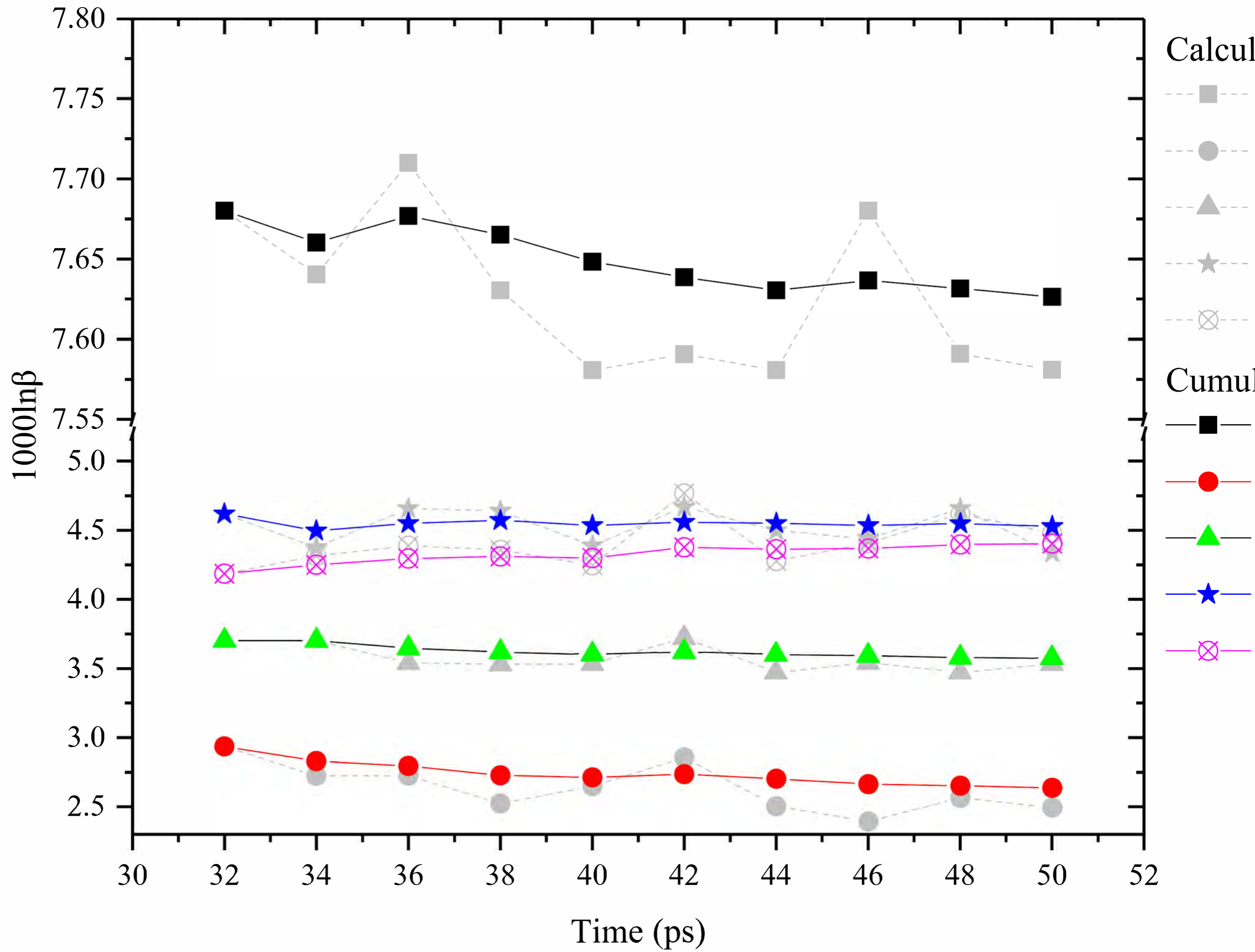


Fig.3

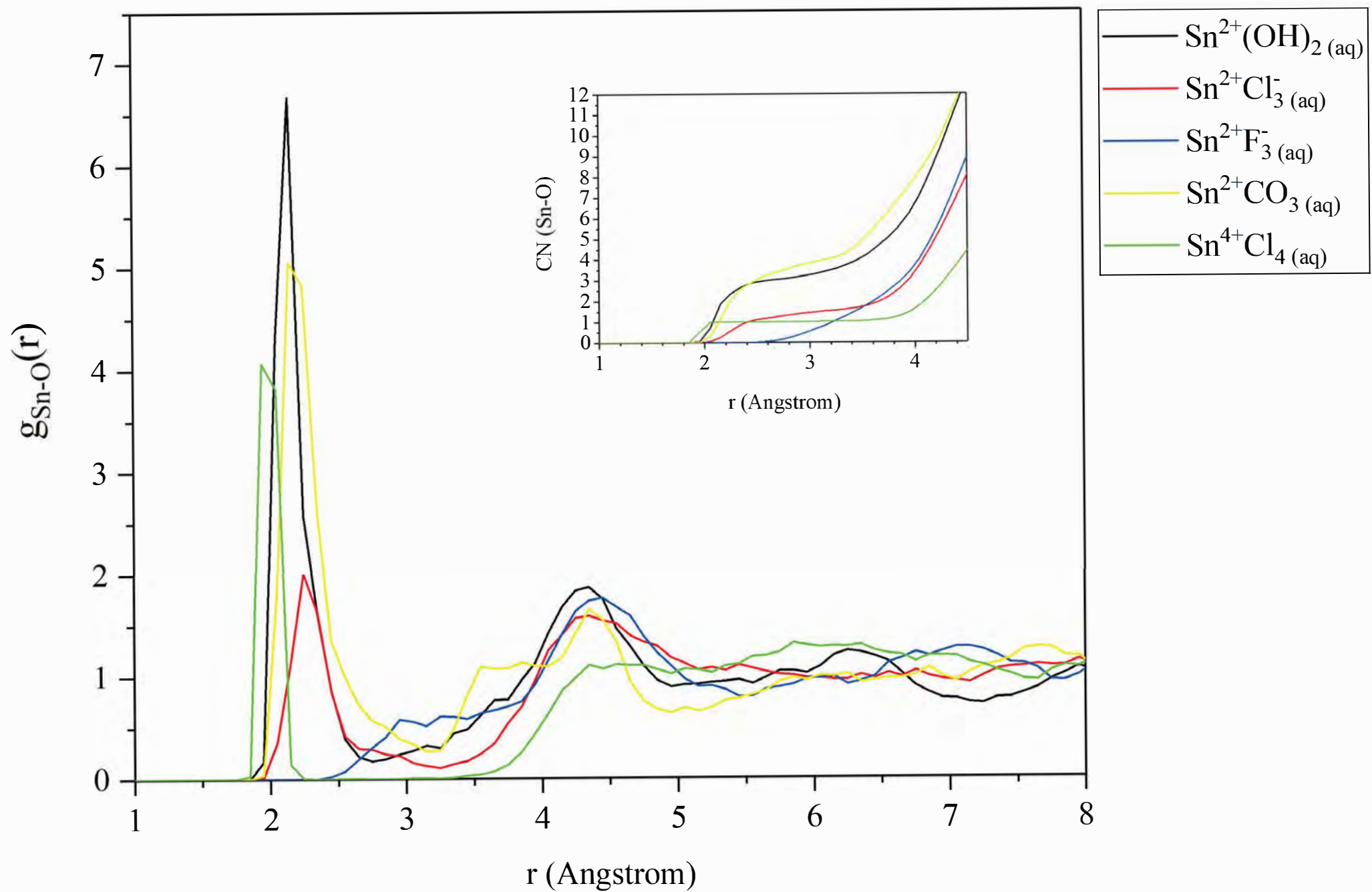




Fig.4

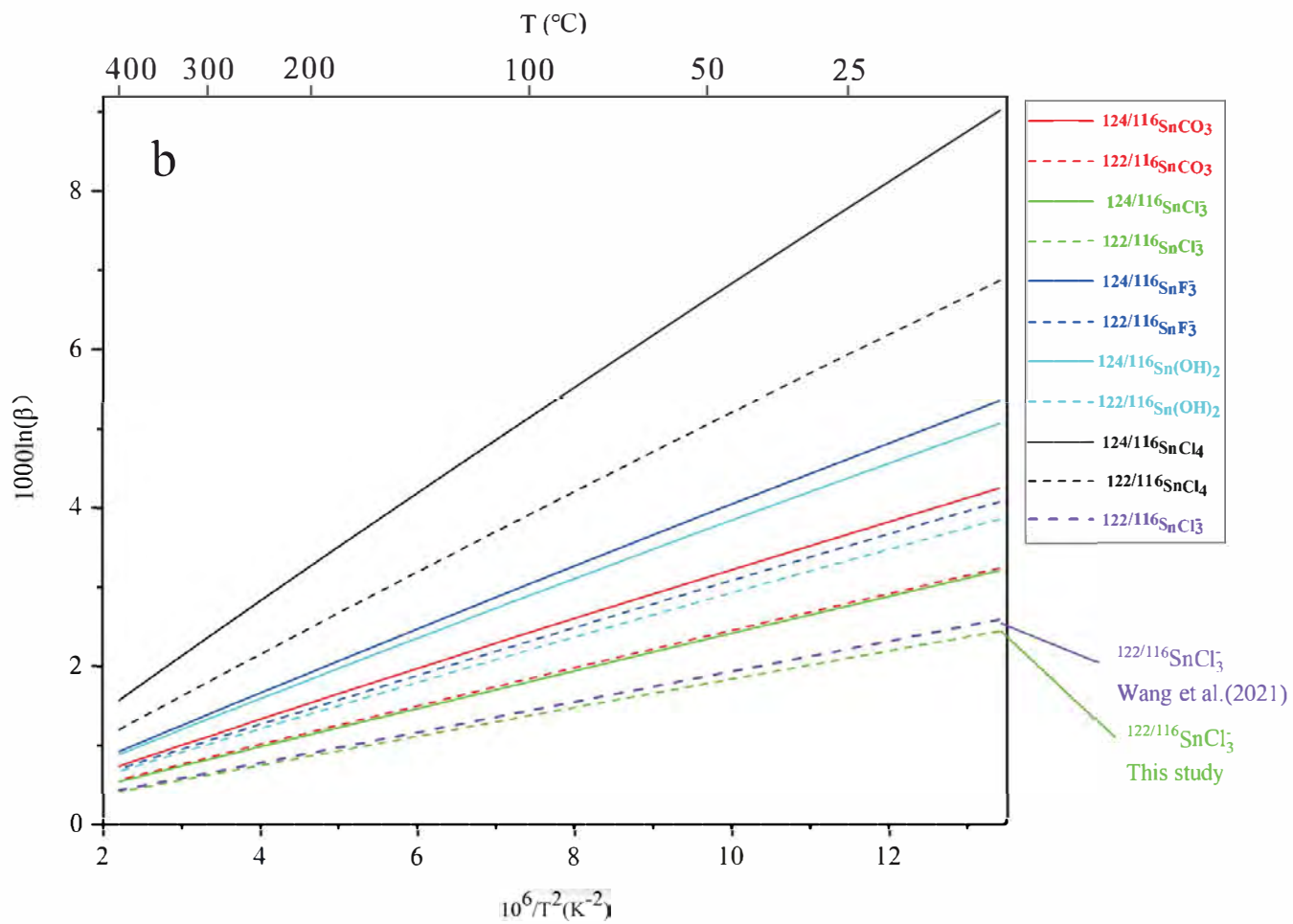
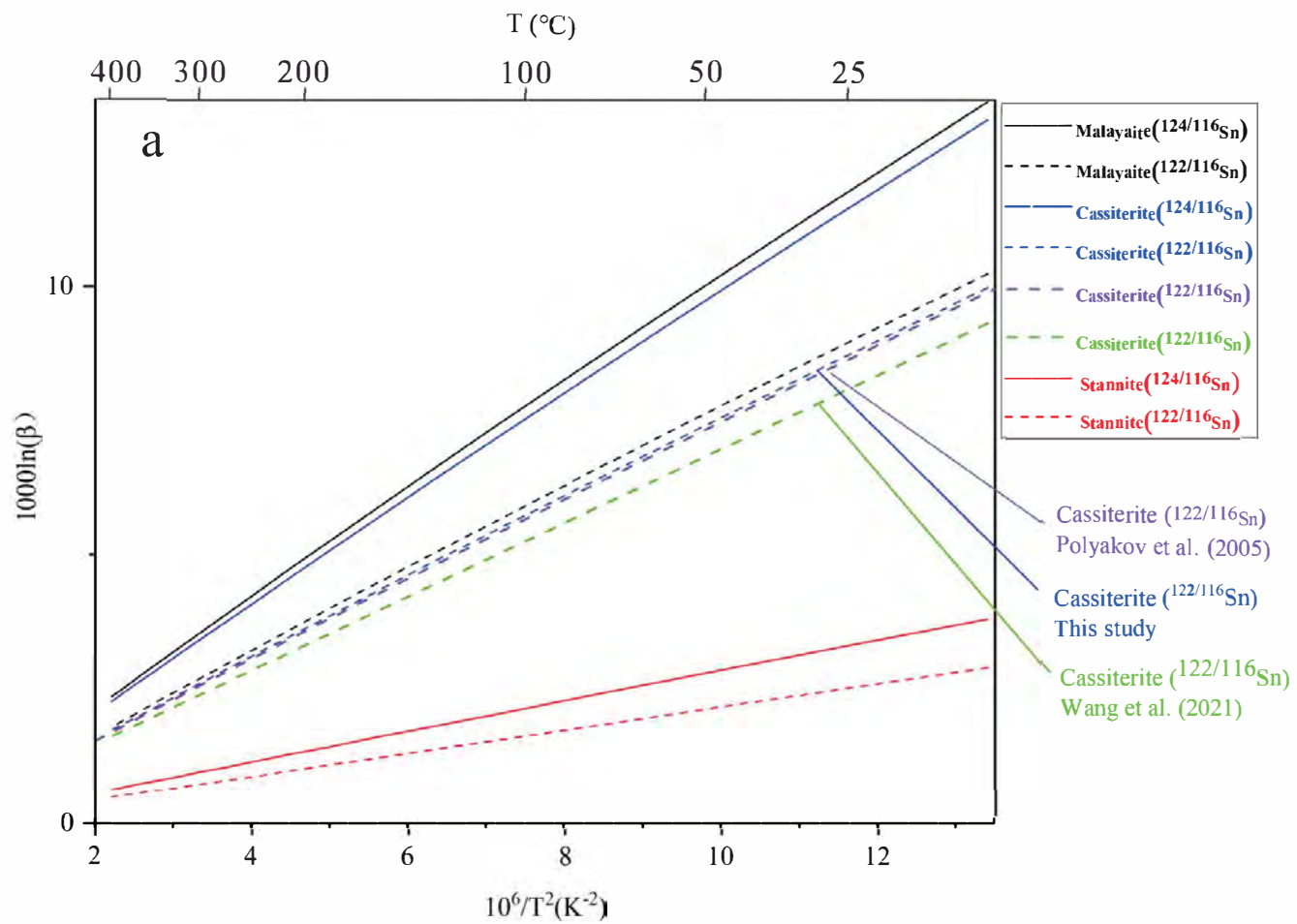


Fig.5

